Z. Angew. Math. Phys. 66 (2015), 149–169
© 2014 Springer Basel
0044-2275/15/010149-21
published online January 10, 2014
DOI 10.1007/s00033-013-0396-z

Zeitschrift für angewandte Mathematik und Physik ZAMP

Stokes flow in a two-dimensional micro-device combined by a cross-slot and a microfluidic four-roll mill

Jing Guan, Jinxia Liu, Xiaoduan Li, Jun Tao and Jingtao Wang

Abstract. The flow structures in a novel microfluidics device (CS-MFRM) combining a cross-slot (CS) and a microfluidics four-roll mill (MFRM) have been investigated through a two-dimensional boundary element method. By changing the volume flow rates at various inlets of a CS-MFRM, diverse flow structures can be generated. Some of them are proposed to be employed to achieve some functions in the fabrication process of anisotropic particles. The stagnant points and eddies in those flows are particularly discussed since they are critical to trap and/or rotate droplets. Energy consumption of eddies generated in branches in some flow structures is also investigated in this paper.

Mathematics Subject Classification (2000). 76D07 · 76T25.

Keywords. Boundary element method · Microchannels · Stagnation points · Flow branches · Stokes eddies.

List of symbols

μ	The viscosity of continuous phase
λ	The viscosity ratio of the droplet to the continuous phase
G	Shear rate
p	Pressure
$\boldsymbol{u}$	Velocity vector
$\boldsymbol{f}$	Surface stress
S_{ij}	Fundamental solution of the two-dimensional Stokes equations
T_{ijk}	Associated stress kernel of the fundamental solution
Q	Volume flow rate in a channel
w_0	Half width of a channel
r_c	Radius of central circular cavity

1. Introduction

Microfluidics has rapidly developed during the past decade and drawn much attention due to its broad potential applications in chemistry, biology, materials, and drug delivery systems [1–4]. Diverse microfluidic devices have been designed to execute various manipulations including the generation of various flow patterns, the generation, deformation, coalescence, and mixing and breakup of droplets[5–10]. As a simple and common device, the microfluidic cross-slot has been employed to trap the particles [11], to investigate the deformation and breakup of droplets [12], and to analyze the structures of the DNA molecules [13,14]. Hellou and Bach [15] investigated the possible Stokes flow structures in four orthogonal channels by covering diverse flow rate distributions and concentrated on the cases that exhibited eddies. However, the cross-slot can only generate few different flow patterns due to the relatively simple geometry. Lee et al. [16] designed a microfluidic four-roll mill (MFRM) which could generate all flow types from the pure extension flow to simple shear flow and to pure rotational flow. Wang et al. [17] investigated the effects of

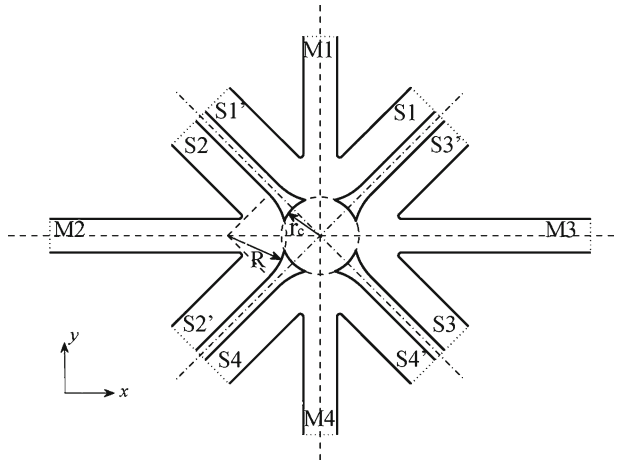

Fig. 1. Illustration of a CS-MFRM

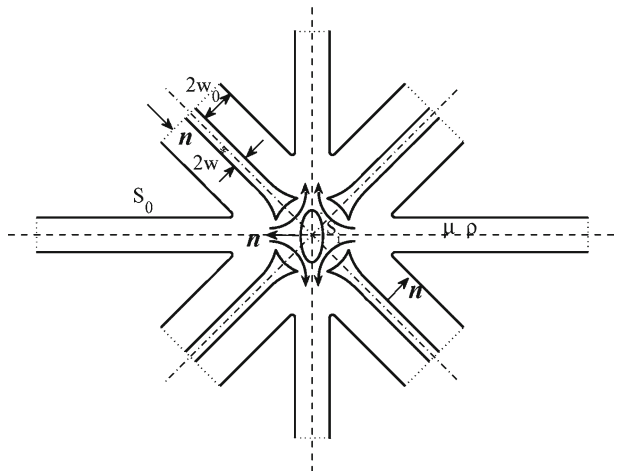

Fig. 2. Illustration of a deforming droplet in a CS-MFRM

the MFRM geometry on the deformation and rotation of droplets through a two-dimensional (2D) spectral boundary element method and found the appropriate size range of the orifice of the central cavity. Due to the flexibility to product various flow patterns, MFRM has been employed to study the tumbling dynamics of DNA [18], the entire phase diagram of motions (tank-treading, tumbling, and trembling) of vesicles in general flows [19], and may have wide potential applications in complex behaviors of the droplet deformations in creeping flows [20].

Lately, Wang et. al. [21] presented a novel microfluidic device (Figs. 1, 2)which is a combination of a cross-slot (CS) and a MFRM and simulated the preparation of anisotropic particles through this device numerically. This new device is named CS-MFRM in which the vertical channels (M1 and M4 in Fig. 1) are the passage of the main drop (MD) to enter or leave the device, the horizontal channels (M2 and M3 in Fig. 1) are for the small droplets (SD) which will be adhered to MD to form patches or compartments, and the other eight inlets (S1–S4 and S1′–S4′ in Fig. 1) are employed to control the flow patterns in the central cavity. The general procedure [21] to fabricate a multi-compartment particle or a patchy particle

is as follows: (1) A main drop is injected into the device through the channel of M1 and trapped at the center of the central cavity (2). One small droplet is transported into the device through the horizontal channel of M2/M3 (3). The small droplet approaches, collides and merges with MD under an extensional flow to form a patch (4). Then, MD will rotate by some angle under the action of a rotational flow (5). Another SD is injected into and merges with MD to form another patch (6). Repeating step 4 and 5 to fabricate an anisotropic particle with multiple patches at expected angles in two dimensions (7). The prepared anisotropic particle is released from the device through the vertical channel of M4.

Due to the complexity of the geometry of CS-MFRM, extremely diverse flow patterns can be generated by varying the flow rates at the various inlets and outlets. It is impossible to discuss them all. Thus, flow structures which might be useful in the fabrication of anisotropic particles will be investigated first in this paper. Further, a bunch of branches in a CS-MFRM and the variation of flow rates in complex channels will easily induce various eddies. These eddies usually appear in some specific positions and might have significant effects on the flows or have some good uses. Shankar [22] studied the eddy structures in two-dimensional Stokes flows in a rectangular cavity. Georgiadou et. al. [23] has investigated the effect of eddies on mass transfer. Microeddies have been employed to trap cells [24] for dynamic single-cell measurement and to trap bioparticles [25] through hydrodynamics for further manipulations. As for CS-MFRM, the existing eddies might significantly affect the preparation process of anisotropic particles, such as the rotation of MD. Thus, in order to know the effects of formed eddies and to employ them to reach some specific goals, we will also investigate various eddies formed in the channels under different flow patterns in this paper.

Through a two-dimensional (2D) spectral boundary element method, a powerful tool to study interfacial dynamics of droplets in microchannels due to its high facility in describing the complex geometries and the various boundary conditions, and the different flow structures with various volume flow rates in a CS-MFRM are investigated. The flow fields in the central cavity of the device are paid particular attention. The distribution of eddies and their influences on the fabrication process of anisotropic particles will also be discussed.

2. Mathematical formulation and numerical method

The configuration of CS-MFRM is depicted in Figs. 1 and 2 in which M1–M4 are the four channels of a cross-slot, and the other eight inlets (S1–S4 and S1′–S4′) are those of a standard MFRM. This micro-device is totally symmetric and the origin of the Cartesian coordinate system is at the center of this device (Fig. 1). All these channels with the same width $2w_0$ are arranged symmetrically around a central circular cavity with a radius r_c. In this paper, we define the half width w_0 as the length scale, and all length-relevant variables are reduced by it. Since the size of a microchannel in a general micro-device is in the micron-scale, the order of magnitude of w_0 and the flow domain is about micron meters. The function of the cross-slot channels is to introduce or release the main drop and small droplets, while the function of the MFRM channels is to adjust the flow patterns in the central cavity. w^* is the half width of four bafflers and equals to $0.4w_0$. When the four inlets (M1–M4) of the cross-slot are blocked, the rest part of this device can produce the entire spectrum of flow types from pure extensional flows to simple shear flows and to pure rotational flows by adjusting the volume flow rates at the eight inlets of the MFRM [16].

It is assumed that CS-MFRM was full of continuous phase (CP) with viscosity μ and density ρ. As shown in Fig. 2, S_0 is the boundary including the wall, inlet and outlet of the micro-device with unit normal vectors $\mathbf{n}$ perpendicular to boundary and pointing inside. The two-dimensional (2D) droplet is driven and deformed by the continuous phase. The governing equations of the external fluid are Stokes equations and the continuity equation

$$-\nabla p + \mu \nabla^2 \boldsymbol{u} = 0, \tag{1}$$

$$\nabla \cdot \boldsymbol{u} = 0, \tag{2}$$

where $\boldsymbol{u}$ is the velocity of CP and p is the pressure. The effect of gravity is neglected in this paper. These equations can also be applied for all droplets in the system. Nonetheless, physical parameters in these equations must be replaced by the corresponding parameters of those droplets, such as the viscosity $\lambda_i\mu$. λ_i is the viscosity ratio of the ith droplet to CP (In this paper, the viscosity of all droplets is the same, i.e., $\lambda_i = \lambda$). The interface of the ith droplet with normal vectors pointing outward is indicated by S_i, and its interface tension and density are γ_i and $\kappa_i\rho$. κ_i is the density ratio of the droplet to CP (In this paper, the interface tension of all droplets is the same, i.e., $\gamma_i = \gamma$). Droplets sizes are specified by their area A_i or equivalently by their diameters $d_i, \pi d_i^2/4 = A_i$. Boundary conditions (BCs) of the velocity $\boldsymbol{u}$ and surface stress $\boldsymbol{f} = \boldsymbol{\sigma} \cdot \mathbf{n}$ on S_i are

$$\boldsymbol{u}_i = \boldsymbol{u}_i^{\mathrm{CP}}, \tag{3}$$

$$\Delta \boldsymbol{f}_i = \boldsymbol{f}_i^{\mathrm{CP}} - \mathbf{f}_i = \gamma\,(\nabla \cdot \boldsymbol{n})\,\boldsymbol{n} + (1-\kappa_i)\,\rho\,(\boldsymbol{g}\cdot\boldsymbol{x})\,\boldsymbol{n}.(i = 1, 2, 3, \ldots\ldots, n) \tag{4}$$

At walls of the microfluidic device, the non-slip BC gives the velocity of CP

$$\boldsymbol{u}_0 = 0, \tag{5}$$

At the inlets and outlets, the undisturbed flows are specified as the parabolic pressure-driven flows. The velocity profile is

$$\boldsymbol{u}_0 = \pm G\frac{w_0}{2}\left[1 - \left(\frac{r_w}{w_0}\right)^2\right]\mathbf{u}, \tag{6}$$

where G is the shear rate at the wall of inlets or outlets; where r_w is the distance of a point in a channel to the central axis of the channel; positive sign is for inlets and negative sign is for outlets. The volume flow rate can be calculated by $Q = 2(w_0^2 G)/3$.

The velocity at a point $\boldsymbol{x}_0$ on the droplet surface and outer boundaries can be described by boundary integral equations (BIE) which are developed from Stokes equations and the continuity equation [26]. The main advantage of the mathematical method is that the discretization involves only the boundary instead of the entire domain which reduces the dimensionality of the problem by one. Since Youngren and Acrivos [27] introduced the boundary integral method in the study of low-Reynolds-number flows, this numerical technique has been employed and developed by many researcher groups [28–33]. Muldowney and Higdon [28] developed a spectral boundary element approach to solve the three-dimensional Stokes equations. Liang and Subramaniam [29] employed boundary element method to compute molecular electrostatics. Pozrikidis [30] introduced the elastic properties into boundary conditions of the boundary integral method in order to investigate the rheology of blood cells, capsules, and so on. Lately, Wang et. al. [32,33] developed a more generalized boundary integral equation (GBIE) which can treat the rheology of multiple emulsions with any internal structures in microchannels with various geometries (see "Appendix"). This GBIE is divided into three rows, the first row defines the outer boundary such as the wall and inlets of the channels, the second row defines the outmost interface of the globules and their numbers m_1, and the third row specifies the diverse internal structures of the globules. When there are no internal structures and m_1 is any positive integer, it is simplified to a BIE to study the deformation and coalescence of simple droplets of any numbers.

In the current paper, since we only investigate the displacement and deformation of simple-emulsion droplets which have no inner daughter droplets in microchannels, the simplified form of GBIE is employed. The velocity at a point $\boldsymbol{x}_0$ on the droplet surface S_i and outer boundaries S_0 can be described by the following boundary integral equation (BIE)

$$\mathrm{LHS} = -\int_{S_0}[\boldsymbol{S}\cdot\boldsymbol{f} - \mu\boldsymbol{T}\cdot\boldsymbol{u}\cdot\boldsymbol{n}]\mathrm{d}S - \sum_{i=1}^{n}\int_{S_i}[\boldsymbol{S}\cdot\Delta\boldsymbol{f}_i - (1-\lambda)\mu\boldsymbol{T}\cdot\boldsymbol{u}\cdot\boldsymbol{n}]\mathrm{d}S \tag{7}$$

when x_0 is on the ith droplet surface $S_i, \mathrm{LHS} = 2\pi\mu(1+\lambda)\boldsymbol{u}(\boldsymbol{x}_0)$; when x_0 is on the outer boundaries $S_0, \mathrm{LHS} = 2\pi\mu\boldsymbol{u}(\boldsymbol{x}_0)$; where n can be any integer. Through Eq. (7), the numerical solutions of $\boldsymbol{u}(\boldsymbol{x}_0)$ on

the surface of the drop can be calculated. S_{ij} is the fundamental solution of the two-dimensional Stokes equations, and T_{ijk} is the associated stress kernel defined by

$$S_{ij}\left(\hat{\boldsymbol{x}}\right) = -\delta_{ij}\ln r + \frac{\hat{x}_i\hat{x}_j}{r^2}, \tag{8}$$

$$T_{ijk}\left(\hat{\boldsymbol{x}}\right) = -4\frac{\hat{x}_i\hat{x}_j\hat{x}_k}{r^4}, \tag{9}$$

where $\hat{\boldsymbol{x}} = \boldsymbol{x} - \boldsymbol{x}_0, r = |\hat{\boldsymbol{x}}|$ and $\boldsymbol{x}$ is any point in the boundary. $\boldsymbol{f}$ on the surface of the drop can be calculated through Eq. (10),

$$2\pi\mu\boldsymbol{u}(\boldsymbol{x}_0) = -\int\limits_{S_0+S_B}[\boldsymbol{S}\cdot\boldsymbol{f} - \mu\boldsymbol{T}\cdot\boldsymbol{u}\cdot\boldsymbol{n}]\mathrm{d}S. \tag{10}$$

The velocity at a internal point $\boldsymbol{x}$ of MFRM (excluding the walls, inlets, outlets, and the droplet surface) can be calculated by the following boundary integral equation [26],

$$4\pi\mu\boldsymbol{u}(\boldsymbol{x}) = -\int\limits_{S_0+S_B}[\boldsymbol{S}\cdot\boldsymbol{f} - \mu\boldsymbol{T}\cdot\boldsymbol{u}\cdot\boldsymbol{n}]\mathrm{d}S. \tag{11}$$

The numerical solution of the set of boundary integral equation and boundary conditions can be achieved through the spectral boundary element method developed by Muldowney and Higdon [28]. Here, the interfaces of the microchannels and droplets are discretized according to the methodology developed by Dimitrakopoulos and Wang [31]. The initial interfaces are divided into a moderate number N_{E} of elements. In each element, there are N_{B} basis points which are in the interior of the element, i.e., Gauss-type points. The Gauss-type points can be derived from the Jacobi polynomials. They are diverse orthogonal polynomials when the parameters α and β take different values. For instance, when $\alpha = \beta = 0$, we have Legendre polynomials. In our calculations, we take $\alpha = \beta = -0.99$.

The total number of the discretized points is defined by $N = N_{\mathrm{E}^*}N_{\mathrm{B}}$. For the CS-MFRM shown in Fig. 1, we take $N_{\mathrm{E}} = 100$. In order to check the effects of the total points number N on the numerical result, N_{B} is changed from 6 to 13 and sequentially N varies from 600 to 1,300. A rotational flow is chosen to testify the effect of N, which can be generated in the central cavity of the CS-MFRM by taking $Q_{Si} = Q_{Si'} = Q(i = 1, 2, 3, 4)$ (Details are stated in Sect. 3.3). The θ in Fig. 3a is the average angular velocity of rotation at the points ($r = 1.0$) in the central cavity. If we consider that the calculated θ when $N = 1,300$ is accurate, we can see the effect of N from the relative error of θ calculated when N varies from 600 to 1,300. By observing the results shown in Fig. 3a, we can see that it is reasonable to assume that the numerical results for $N = 1,300$ is the accurate one. When N is larger than 1,000, the results change very little. Thus, in order to reduce the calculation amount and meantime to ensure the necessary accuracy of results, we choose $N_{\mathrm{B}} = 10$, i.e., $N = 1,000$ in this paper.

In order to determine the evolution of droplet shape, an explicit time-integration algorithm is employed to solve the kinematic condition at the interface

$$\frac{\mathrm{d}\boldsymbol{x}}{\mathrm{d}t} = \boldsymbol{u} = u_n\cdot\boldsymbol{n} + u_t\cdot\boldsymbol{t}, \tag{12}$$

where u_n and u_t are normal and tangential components of the velocity $\boldsymbol{u}$, respectively, and $\boldsymbol{t}$ is the tangential vector of the droplet interface. In our studies, high-order schemes like fourth-order Runge–Kutta method are employed to lower the numerical error associated with the time integration.

Deformation parameter $D = (L - S)/(L + S)$ is employed to describe the droplet deformation, where L and S are the lengths of the major and the minor axes of the droplets, respectively. The characteristic length of this 2D micro-device is in the micron-scale. Comparing to interfacial tension and viscous forces, the Bond number which indicates the relative importance of gravity to interfacial tension is far less than one [34]. Thus, in this paper, effects of gravities and buoyancies are neglected.

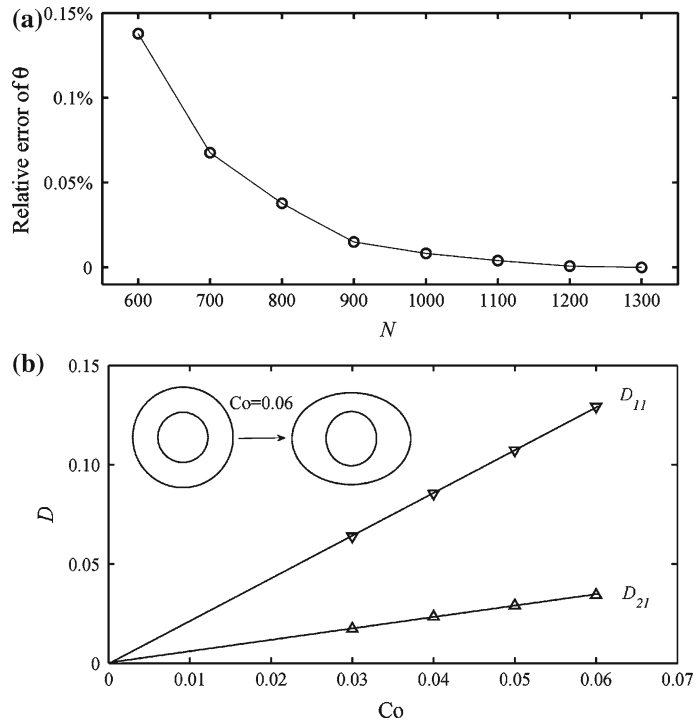

FIG. 3. **a** Effects of the total points number N on the numerical result. **b** Validation analysis of our numerical method by repeating Stone and Leal's results [35]

Validation of our numerical model and code has been done by successfully repeating the results of Stone and Leal [35] (see Fig. 3b) for the deformation of a concentric double-emulsion globule under an axisymmetric extensional flow (also see "Appendix"). Although we investigate only the deformation and displacement of simple droplets in this paper, our numerical model and code are more generalized and applicable for rheology investigation of multiple emulsions with any internal structures [32,33]. Equation 7 is only a simplified form of our GBIE (see "Appendix") as we mentioned in the previous paragraph. In addition, due to the geometry complexity of the CS-MFRM, there is no experimental study of the droplet deformation in such a complex micro-device. Thus, repeating Stone and Leal's results will be effective to validate our numerical model and code employed in this paper.

D_{11} and D_{21} in Fig. 3b are the deformation parameter at equilibrium of the outer and inner interface of a concentric double-emulsion globule, respectively. As shown in Fig. 3b, by employing the same infinite extensional flow as that of Stone and Leal [35], and the same relevant parameters such as $\lambda = 1.0$ and the radius ratio of the inner droplet to the globule $k_{21} = 0.5$, we calculate D_{11} and D_{21} for various C_o as shown in Fig. 3b, where $C_o = r_{11}G\mu/\gamma$ is the capillary number based on the globule (r_{11} is the radius of the globule.). Following results are obtained: $C_o = 0.03, D_{11} = 0.064$, and $D_{21} = 0.018; C_o = 0.04, D_{11} = 0.086$, and $D_{21} = 0.024; C_o = 0.05, D_{11} = 0.107$, and $D_{21} = 0.029$; and $C_o = 0.06, D_{11} = 0.129$, and $D_{21} = 0.034$. These results are totally consistent to those of Stone and Leal [35], which fully proves that our numerical method is valid.

In the calculations, w_0 is used as the length scale; when the volume flow rate Q is equal to $2(w_0^2)/3$, the shear rate is unit, which is selected as the scale G_0; thus, the time is scaled with the flow time scale G_0^{-1}; the scale of the flow rate will be $w_0 G_0$; the scale of the volume flow rate will be $w_0^2 G_0$. All physical variables in this paper are reduced based on scales above. Thus, the geometry and flow parameters in this paper are specified. If the half width of all channels $w_0 = 1$, we have $w* = 0.4$, $r_c = 2.29$, and $R = 3.46$.

The physical properties of fluids are the radius of MD $r_{\mathrm{MD}} = 0.75, \lambda = 6.0$, and $\gamma = 5$. Also, the volume flow rate Q is fixed to 0.667.

3. Flow structures

In this section, we will discuss the effects of flow rates and directions at inlets of a CS-MFRM on its internal flow structures and investigate the relationship between the flow structures and the fabrication of anisotropic particles. In the following figures, arrows indicate the entering or leaving of fluids, which only show the flow direction and have no indication of the magnitude of the flow rates. The sign of the volume flow rate of each stream is always positive, and its direction is indicated by the corresponding arrow. No arrows in a channel indicate that there is no significant flow in that channel or the inlet of that channel is closed. The following contents are arranged according to the operating sequence of the process to fabricate anisotropic particles.

3.1. Transporting the main drop

In the process to fabricate anisotropic particles, the first operation is to ensure that the main drop could be easily transported into the central cavity of a CS-MFRM. One of the flow structures that could transport MD to the right place is shown in Fig. 4a. The fluids which carry a MD will be injected into the device through the inlet M1 and then flow out through M2 and M3. All others inlets are closed. In order to retain MD on the vertical central axis, the whole flow field is symmetric, i.e., $Q_{\mathrm{M1}} = 2Q_{\mathrm{M2}} = 2Q_{\mathrm{M3}} = Q$.

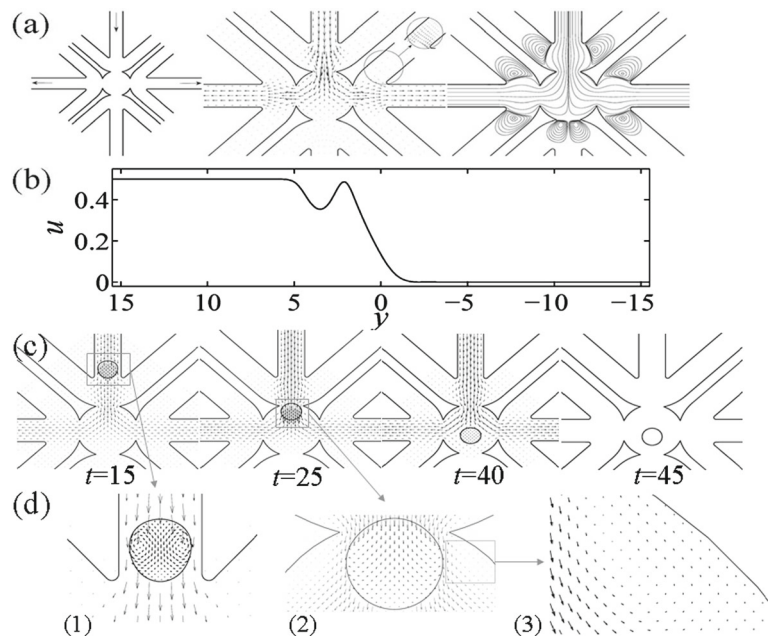

FIG. 4. **a** Flow structure in terms of velocity vectors and streamlines to transport MD into the central cavity. **b** The velocity on the vertical axis. **c** Snapshots of a transporting droplet in a CS-MFRM, and the corresponding flow fields in terms of velocity vectors (in a reference frame fixed to the immobile wall). **d** Enlarged views of the internal flows (4d-1 and 4d-2 are both in the reference frame fixed to the lead edge of the drop) for the droplets (at $t = 15$ and $t = 25$), and the enlarged view (4d-3) of the right eddy generated when the droplet blocks the orifice of the central cavity

This flow configuration is similar to that in a T junction in which a stagnant point exists, and the velocity on the vertical axis will decay to zero near that point. As shown in Fig. 4b, the velocity u reduces rapidly in the central cavity, which facilitates the control of MD to stay inside the central cavity. It is the reason that we do not choose a simpler flow configuration, i.e., a straight flow that enters from inlet M1 and leaves through M4 in which MD might easily miss the landing point and leave the device if without a careful control. During this process, the existence of multiple branches whose entrances are closed will generate some eddies (Fig. 4a) which consume many energies of the flow. The process that a MD is transported into the central cavity is shown in Fig. 4c (The flow fields in Fig. 4c are in terms of velocity vectors in a reference frame fixed to the immobile wall). Initially, this MD moves in the straight channel of M1 with a relatively high velocity and its shape is like a bullet. Its internal flow (for $t = 15$), in terms of velocity vectors in a reference frame fixed to the lead edge of the drop, is shown in Fig. 4d-1. It is clear that there are internal circulations (like two parallel eddies) in the drop. The speed of MD will reduce a little before entering the central cavity since branches S1′ and S1 enlarge the cross-section of the channel. Then, it recovers quickly when MD moves through the window orifice of the central cavity. After it gets into the cavity ($t = 25$), its speed begins to decay and falls down to zero ($t = 40$) rapidly. During this period (from $t = 25$ to 40), the shape of MD is not like a bullet, but a little compressed in the vertical direction as the speed of the front edge is slower. Its internal flow (at $t = 25$) is shown in Fig. 4d-2. Then, the flow is stopped at $t = 40$. MD will retract back to spherical and stay in the central cavity ($t = 45$). Of course, if an exact location at the center of the cavity is needed, further adjustment through subtle flow controls must be done. The velocity vectors shown in Fig. 4c show that the effect of the droplet on the flow field in a CS-MFRM is limited. When $t = 15$ or $t = 40$, there are no evident differences between flow fields shown in Fig. 4a, c. However, when $t = 25$, as the droplet blocks the orifice of the central cavity, there are two small eddies formed by the both sides of the droplet, which could be seen in the enlarged view shown in Fig. 4d-3.

Through the flow structure shown in Fig. 4, it is still not convenient to locate the main drop exactly at the center point since the stagnant point of the flow is at the bottom of the central cavity. Also, channels of M2 and M3 are designed to import the small droplets. Using them as the exits of fluids seems not so convenient. Thus, a new flow structure is designed to overcome such disadvantages as shown in Fig. 5. Channels of M1, S4, and S4′ are employed to import fluids simultaneously ($Q_{S4} = Q_{S4'}$), and channels of S2′ and S3 are employed as the exits of fluids ($Q_{S2'} = Q_{S3}$). When the ratio of the volume flow rates Q_{S4}/Q_{M1} is very small, the stagnant point is located at the lower half of the central cavity. Along with the increment of this ratio Q_{S4}/Q_{M1}, the position of the stagnant point gradually elevates. As shown in Fig. 5e, when Q_{S4}/Q_{M1} is equal to 0.47, the stagnant point is just located at the center point.

3.2. Extensional flows

After locating MD at the center of the central cavity, the second step is to transport small droplets (SD) into the cavity through the channels of M2 and M3, and to make them collide with MD to generate patches in MD. Extensional flows are the promising flow structures which could drive the small droplets and cause the head-on collision between them and MD. In a CS-MFRM, channels of M2 and M3 are designed to introduce SD into the device. They could be employed alternately to transport small droplets composed of distinct materials. The flow structure shown in Fig. 6a is one of the fields of extensional flows. It is totally symmetric about the vertical axis. Thus, $Q_{M2} = Q_{S2} = Q_{S2'} = (1/6)Q, Q_{M3} = Q_{S3} = Q_{S3'} = (1/6)Q, Q_{S1} = Q_{S1'} = (1/4)Q$, and $Q_{S4} = Q_{S4'} = (1/4)Q$. The process that a SD is transported into the central cavity and collides with MD is shown in Fig. 6c. Initially, MD is trapped at the device center which is also the stagnant point of the extensional flow, and SD is transported through the channel of M2. During the whole process, MD almost doesn't move, but deform more of less. The speed of SD when it moves in channel of M2 is steady and rises rapidly when the streams in channels of M2, S2, and S2′ converge (Fig. 6b). In the central cavity, the speed of SD drops down quickly. Finally, SD and MD

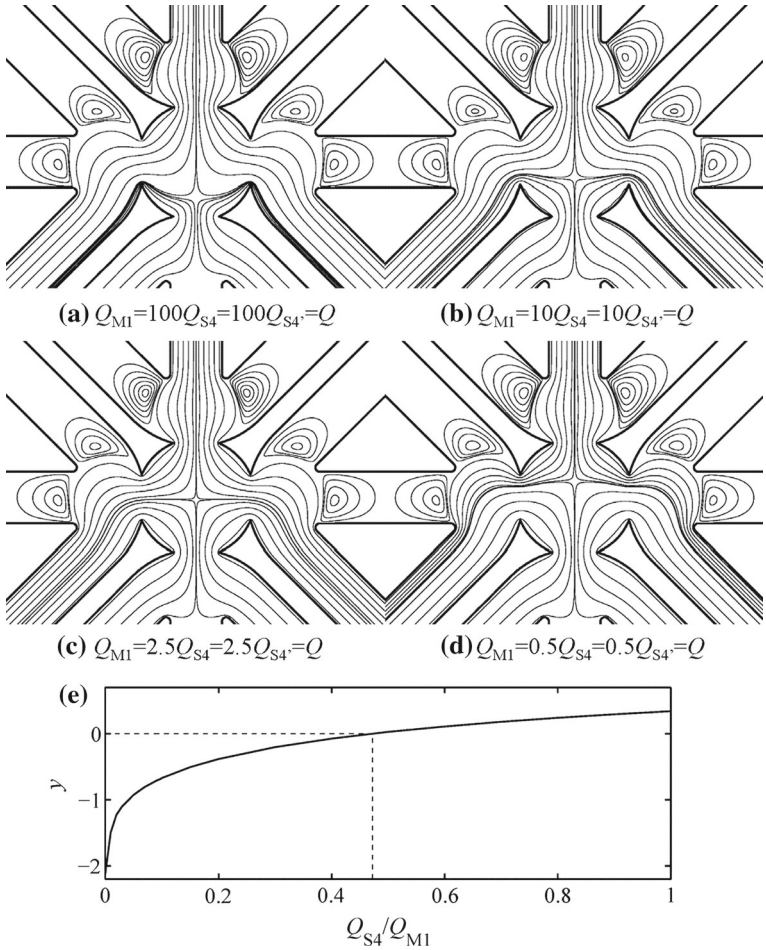

FIG. 5. Flow structures in which the stagnant point can be adjusted by changing the volume flow rate of inlets S4 and S4′. **a**–**d** Flow structures with various ratio of Q_{M1} to Q_{S4} and $Q_{S4'}$. **e** The y coordinates of the stagnant point versus the ratio Q_{S4}/Q_{M1}

collide around the stagnant point where the velocity is zero. The velocity vectors shown in Fig. 6c show that the effect of the droplets on the extensional flow in the CS-MFRM is very limited (almost no evident effects). When $t = 10$, SD is far away from MD, and MD reaches a deformed shape at equilibrium. At this time, there are four symmetric eddies formed in MD, which is a well-known flow pattern for a deformed droplet at equilibrium under an extensional flow [32–34]. When $t = 30$, SD is so close to MD that the collision almost happens. At this moment, the asymmetric velocity vectors in MD show that MD moves a little to the right of the central point, which is caused by the squeeze of SD.

Flow structures which could generate an extensional flow in the central cavity are diverse due to the geometric complexity of a CS-MFRM. As shown in Fig. 7, several typical flow structures are depicted and compared. Figure 7a shows an extensional flow in terms of velocity vectors and streamlines in a common MFRM, and Fig. 7b–d is three flow structures which also generate extensional flows in the central cavity of a CS-MFRM. For all of four cases, the total volume flow rates entering the central cavity are all equal to Q, and the flow rate in each channel is equal. Figure 7a, b compares the extensional flows in a common MFRM to that in a CS-MFRM. They are very similar in the central cavity. However, four more branches (M1–M4) in a CS-MFRM instead of smooth arc walls in a MFRM result in many energy

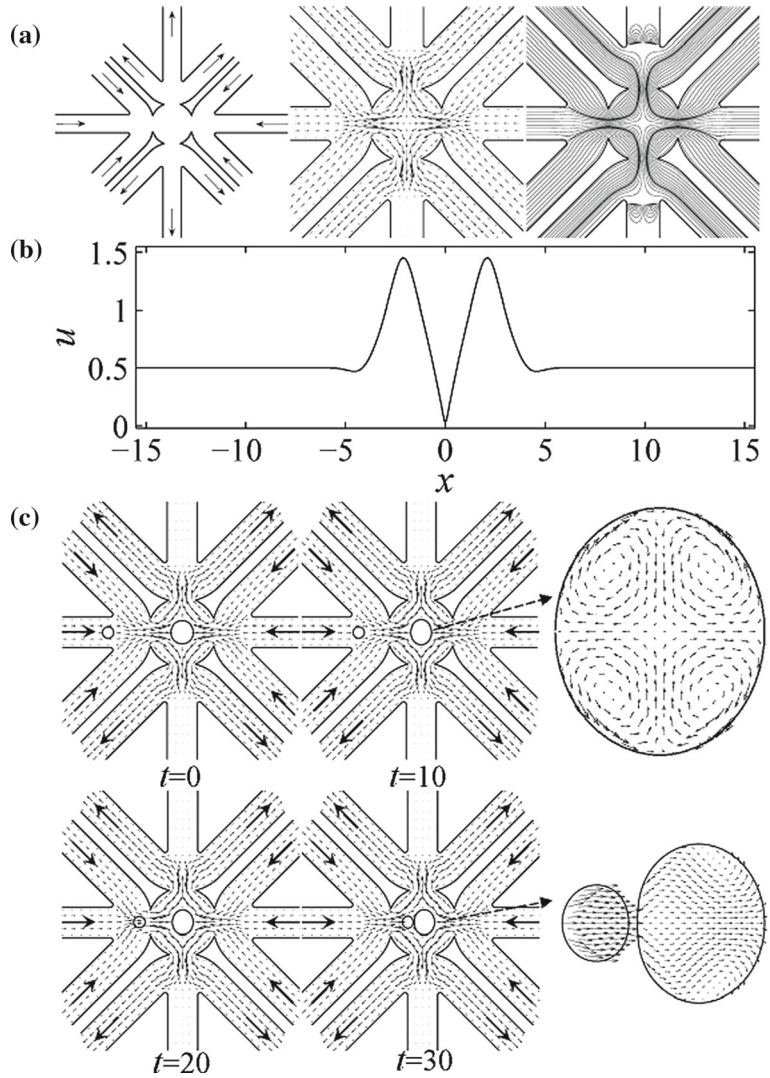

FIG. 6. Extensional flow: $Q_{\mathrm{M2}} = Q_{\mathrm{S2}} = Q_{\mathrm{S2}'} = (1/6)Q, Q_{\mathrm{M3}} = Q_{\mathrm{S3}} = Q_{S3'} = (1/6)Q$, $Q_{\mathrm{S1}} = Q_{\mathrm{S1}'} = (1/4)Q$, and $Q_{\mathrm{S4}} = Q_{\mathrm{S4}'} = (1/4)Q$. **a** The extensional flow in terms of velocity vectors and streamlines **b** The velocity on the horizontal axis **c** snapshots of the collision of SD and MD under an extensional flow and the corresponding flow fields in terms of velocity vectors

consumptions for the former since four pairs of eddies form in the branches (Fig. 7b). This can be seen in Fig. 7e which shows the time change of the deformation parameter D of the same main drop for all four cases. Although the curves are very similar for case (a) and case (b), the difference can still be seen in the insertion of Fig. 7e. Less deformation in case (b) indicates that eddies consume some flow energies. Comparing Fig. 7c to Fig. 7d, a similar conclusion can be obtained. In Fig. 7c, all channels are filled with fluids, while in Fig. 7d only four main channels (M1–M4) are employed to generate the extensional flow. Eight symmetric eddies are generated in the branches (Fig. 7d), which consume some flow energies and cause the lower deformation parameter D in Fig. 7e. These eddies formed in the channels with zero flow rates are similar to those formed in Hellou and Bach's works [15].

Another issue that must be mentioned is the following: in a deformed MD, internal circulations are induced by the outer extensional flow. The internal circulation is vital to the location of a patch, especially

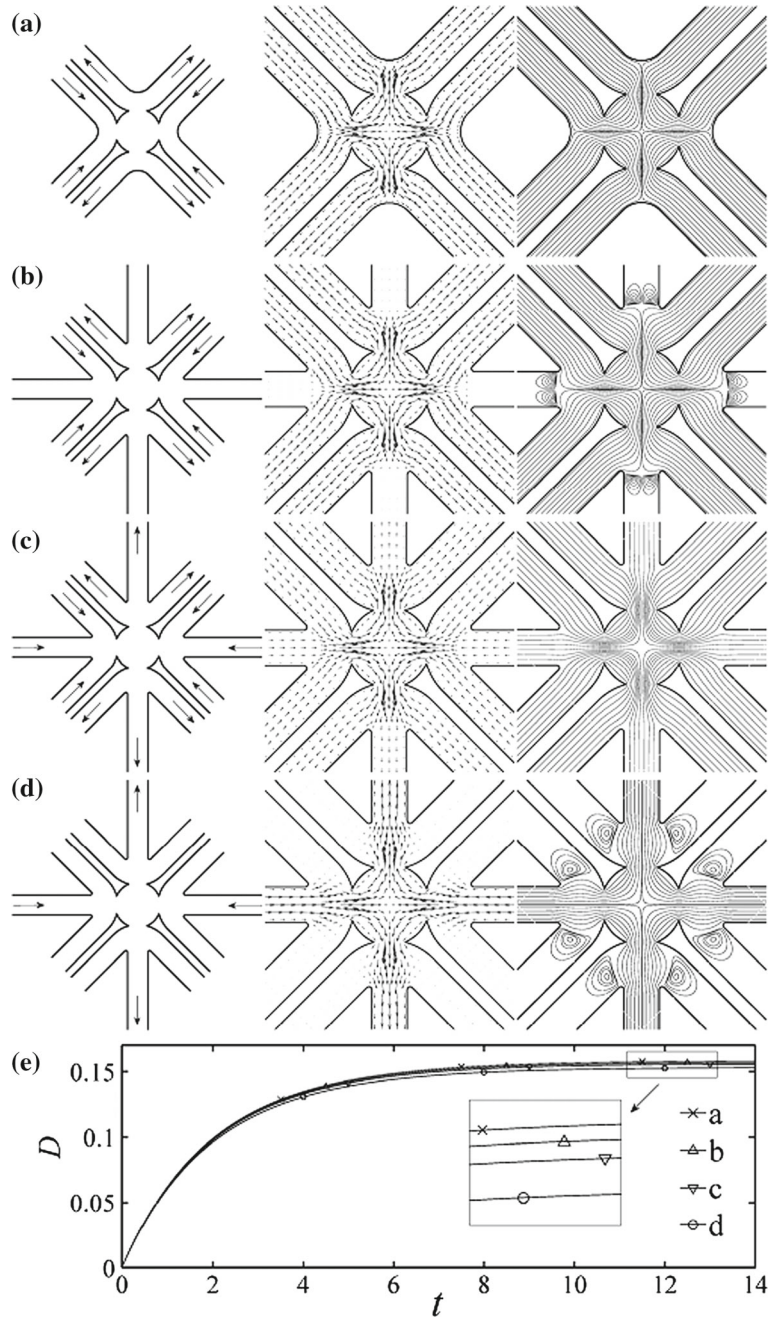

FIG. 7. **a** Extensional flows (in velocity vectors and streamlines) in a common MFRM. **b**–**d** Three flow structures (in velocity vectors and streamlines) which generate extensional flows in the central cavity of a CS-MERM. **e** Deformation parameters D of MD for various flow structures (**a**–**d**) versus time

in the process to fabricate a particle with multiple patches since the fabrication is an iterative process and the earlier patch in a MD will move along with the inner flows induced by a later extensional flow. Thus, the time of the operation step that a SD is driven by an extensional flow to approach MD, the less the better, which is the reason that we design a "propelling flow" in Sect. 3.4.

3.3. Rotational flows

The rotational flow is critical in the fabrication of anisotropic particles with multiple patches at expected angles. It can be generated by employing the flow structures shown in Fig. 8a, b, and it is actually a big and symmetric eddy in the central cavity. Through this flow, the main drop can be rotated by some expected angle and then attach the next patch at the targeted location.

As shown in Fig. 8a, b, when $Q_{\mathrm{Si}} = Q_{\mathrm{Si}'} = Q(i = 1, 2, 3, 4)$, similar rotational flows can be generated both in a MFRM and in a CS-MFRM. However, four eddies form in the four branches (M1–M4) of a CS-MFRM (Fig. 8b). The rotation speeds of the four eddies are very low, which can be seen in Fig. 8c. Since the channels of M2 and M3 are closed, the flow velocity in them is close to zero almost everywhere except for cellular flow region near the junctions that connect the channels of M2 and M3 to the device. In Fig. 8c, A and B are the centers of two small eddies, and the dash line indicates the exact position of the connection that connects the channel of M3 to the device. Since the function of channels of M2 and M3 is to transport small droplets, the two eddies might be used to trap the next small droplet (SD) waiting for the next coalescence when the main drop with some patches is rotating [21]. At the end of the rotation of MD, SD is able to start to move toward MD under the extensional flow shown in Fig. 6c from point A or B. Or else, SD must start its journey approaching MD from the inlet M2 or M3. Thus, trapping SD at point A or B may save time that SD moves from the inlet M2 or M3 to the point A or B in the fabrication process of anisotropic particles [21].

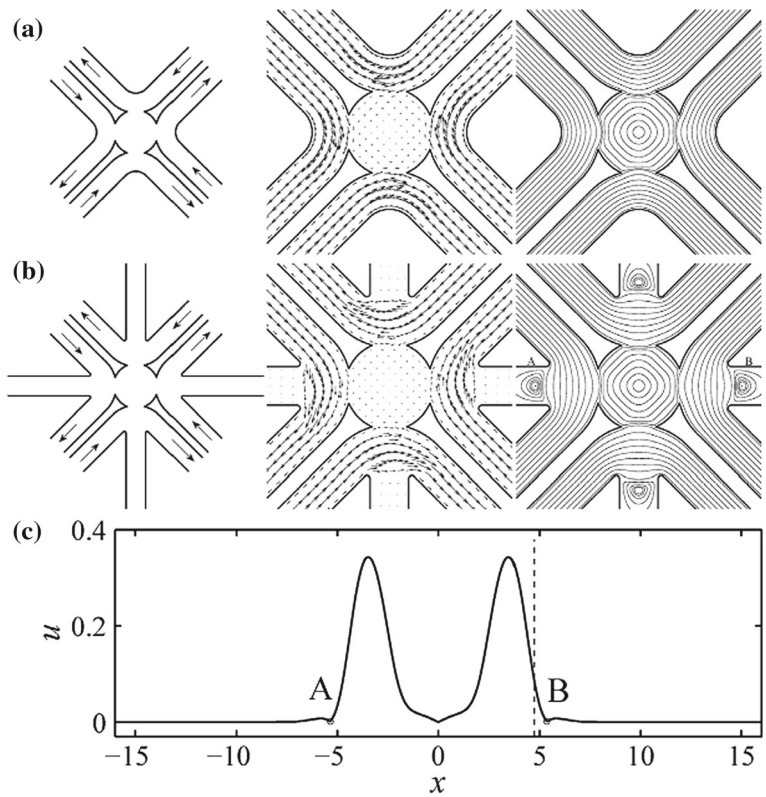

FIG. 8. **a** Rotational flows (in terms of velocity vectors and streamlines) in a MFRM. **b** Rotational flows (in terms of velocity vectors and streamlines) in a CS-MFRM. **c** The linear velocity on the horizontal axis for case (**b**)

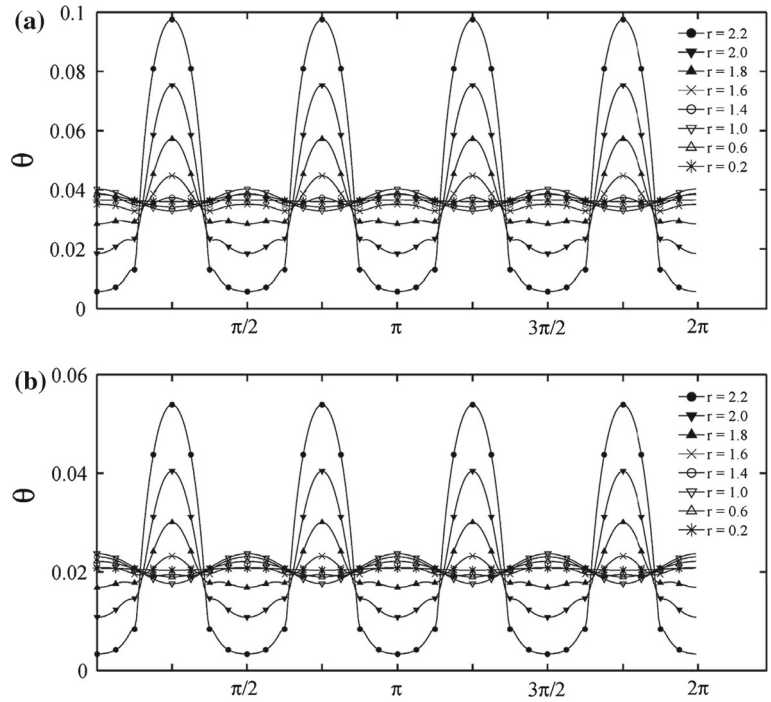

FIG. 9. Distributions of the angular velocities along the circle with various radii in the central cavity. **a** In a MFRM. **b** In a CS-MFRM

As shown in Fig. 8c, the linear velocity of the rotation drops down rapidly in the central cavity. As we know, the corresponding angular velocity is expressed as the quotient of the linear velocity divided by its corresponding radius. Generally, the angular velocity at each point of the flow field should be uniform for a standard rotational flow. Is it still true for the rotational flows generated in a MFRM and in a CS-MFRM? As shown in Fig. 9a, the dependence of the angular velocity of a rotational flow in a MFRM on the radius r of a circle and on the position along the circle is clarified. It is obvious that the angular velocity along a circle with a radius r is not constant, but fluctuated periodically [17]. However, the amplitudes of fluctuation of the angular velocities decrease and the fluctuation curves converge when the radii of the circles shrink. Thus, the angular velocities θ will gradually approach a constant from the edge to the center of the central cavity, which means the flow pattern is close to a standard rotational flow near the center of the central cavity. As shown in Fig. 9a, θ declines along with the decreasing radius and reaches an approximate constant when the radius is less than about 1.4. Above this approximate critical radius, the curves show huge fluctuations. The situation in a CS-MFRM is very similar to that in a MFRM. The only difference is that values of the angular velocity are significantly reduced. This is caused by the energy consumption of the four eddies in the channels of M1–M4.

As shown in Fig. 8b, four eddies form in the channels of M1–M4 when a rotational flow is generated in the device and four inlets M1–M4 are closed. These four eddies consume many energies of the flow as shown in Fig. 9. Thus, if the four inlets M1–M4 import fluids together with other inlets, what kinds of rotational flows can be generated? The results are shown in Fig. 10. Since the whole flow field is totally symmetric, we just use the relation between Q_{S1} and Q_{M1} to show the obtained flow structures. When $Q_{S1} = 100Q_{M1} = Q$, the flow rate in channel of M1 is much less than that in channel of S1. Thus, an eddy forms near the junction due to the severe block by the flow in channel of S1 (Fig. 10a). By the same token, when $Q_{S1} = 0.01Q_{M1} = Q$, an eddy forms in channel of S1 near the junction due to the severe

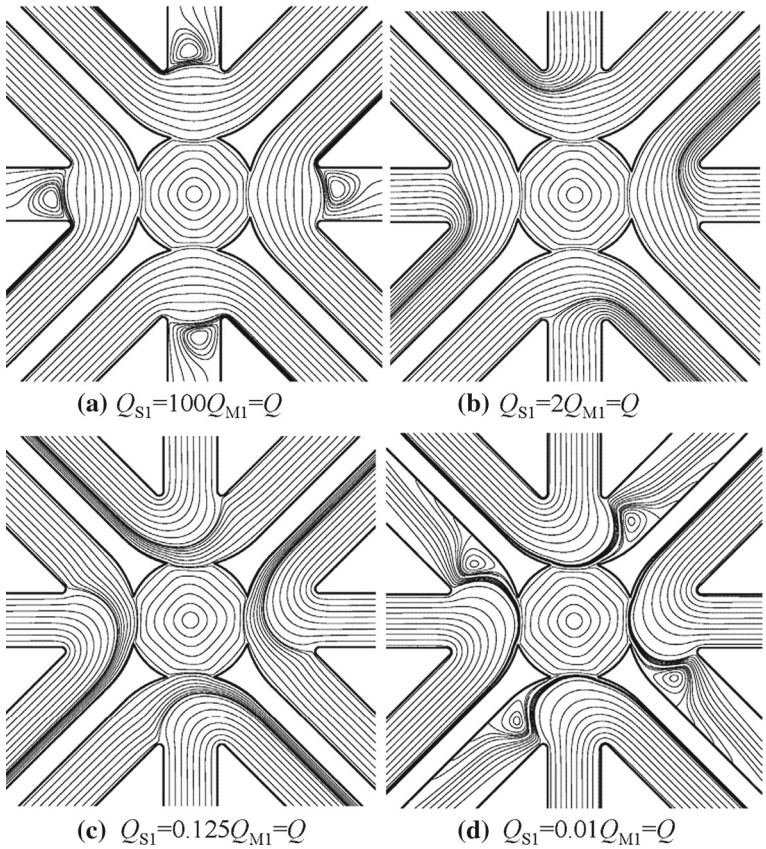

FIG. 10. Rotational flow structures in terms of streamlines when the four inlets M1–M4 import fluids together with inlets S1–S4. **a**–**d** Rotational flow structures for various ratios of Q_{S1} to Q_{M1}

block by the flow in channel of M1 (Fig. 10d). These eddies formed in the channels with low flow rates are similar to those formed in Hellou and Bach's works [15]. When the ratios of Q_{S1} to Q_{M1} are appropriate, smooth rotational flow structures can be generated (Fig. 10b, c).

3.4. Transporting small droplets

In the process to fabricate anisotropic particles, as it is stated in Wang et al.'s work [21], the extensional flow and rotational flow are employed alternately to achieve the adherence of SD to MD and to adjust the location of the adherence. For the fabrication of particles with multiple patches, this alternation of flows will repeat several times. However, since the main drop can only be solidified at the end of the whole process of fabrication, the patches located earlier will move in MD along with the inner circulation induced by the next extensional flow which drives the next SD approaching MD. Thus, if the next SD is closer to MD when the next extensional flow starts, the patches in MD will move less and the location of patches will be controlled more easily and precisely. In order to reach this goal, the following flow structure called "propelling flow" is designed as shown in Fig. 11a, in which M2 and M3 are the inlets ($Q_{M2} = Q_{M3} = Q$), and S2, S2′, S3, and S3′ are the outlets of the fluids. Meanwhile, although the intensity is very small, four eddies form in the central cavity. They further generate a small extensional flow in the vicinity of the center point. By employing this flow structure, the small droplet can be transported

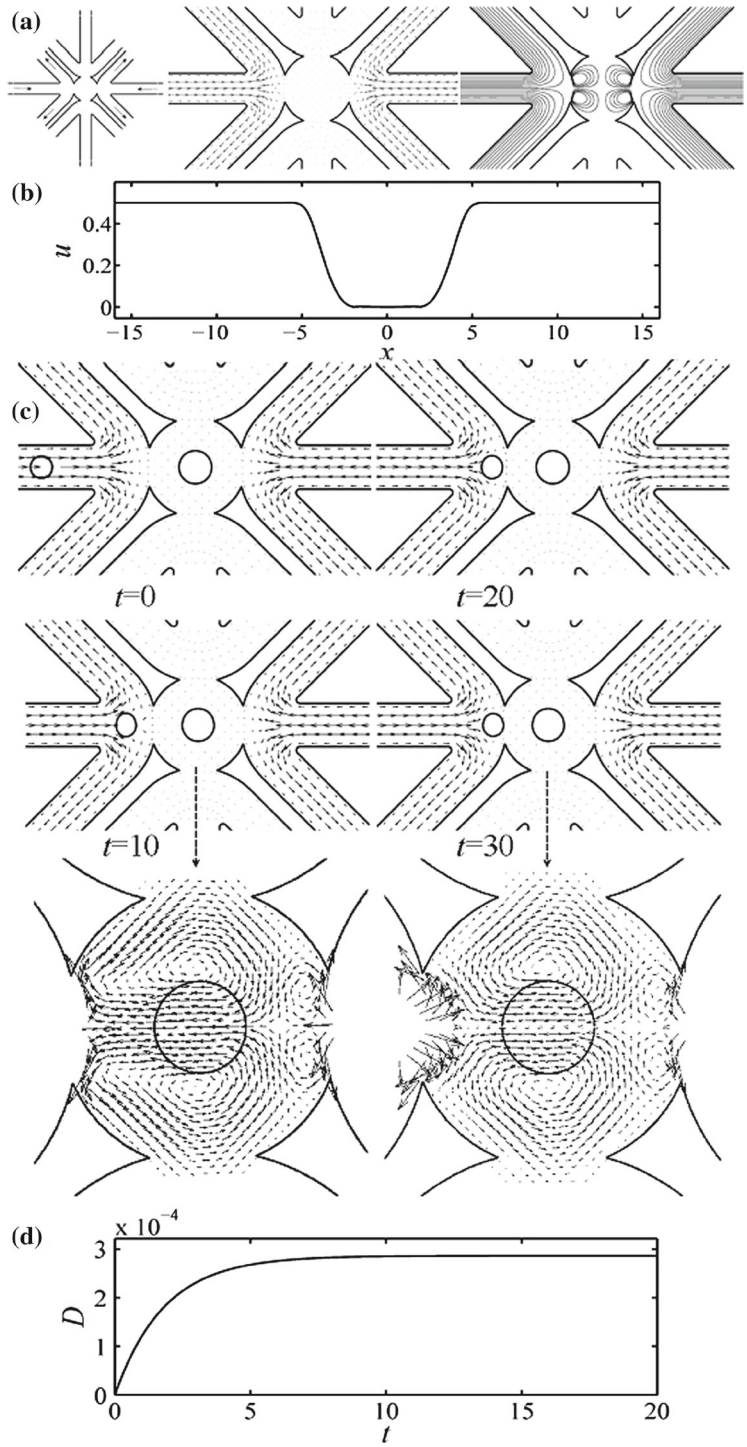

FIG. 11. **a** Propelling flow in terms of velocity vectors and streamlines. **b** The velocity on the horizontal axis. **c** Snapshots of the process to transport a small droplet to the edge of the central cavity and the corresponding flow fields in terms of velocity vectors. **d** Deformation parameters D of MD trapped at the central cavity under the propelling flow versus time

to the edge of the central cavity (Fig. 11c). Meantime, the main drop trapped in the central cavity will almost not deform and will not induce inner circulations since the flow in the central cavity is too weak to be perceived (Fig. 11b). As shown in Fig. 11d, the order of magnitude of deformation parameter D at equilibrium is only 10^{-4}, which can be neglected comparing to $D(10^{-1})$ shown in Fig. 7e. Thus, the alternations of flows in a cycle of the fabrication process could be extensional flows, rotational flows, and propelling flows.

For a propelling flow, the flow in the central cavity is very weak. Nevertheless, by comparing Fig. 11a to 11c, we can see the difference of flow fields with and without droplets inside the central cavity. When there are no droplets, the flow field has four symmetric eddies (Fig. 11a); when there are SD and MD in this micro-device, the flow field becomes asymmetric due to the approaching of SD toward the MD from the left side (Fig. 11c: $t = 10$ and $t = 30$). The closer the distance from the SD to MD is, the more asymmetric the flow field is. The two eddies on the right side are compressed. The left two are enlarged, and move to the topside and bottom-side of the MD. Thus, the MD moves to the left side a little bit although this displacement is too small to be perceived.

Figure 11c is similar to Fig. 6c. However, due to the substantial differences of the flow patterns for these two figures (an extensional flow for Fig. 6c and a propelling flow for Fig. 11c), the movement of the SD and the deformation or the MD are totally different. For Fig. 6c, driven by an extensional flow, SD is able to approach and finally collide with MD in the central cavity; while, for Fig. 11c, driven by a propelling flow, SD is able to approach MD, but it will stop at the orifice of the central cavity and cannot collide with MD. Another difference is that for Fig. 6c, MD is sheared directly by the extensional flow and will have relatively large deformation; while, for Fig. 11c, MD is sheared by a very weak extensional-like flow which is induced by the propelling flow and will deform very slightly (This is also stated in the previous paragraph).

3.5. Other typical flow structures

Besides the flow structures investigated above, there are still many different flow patterns which cannot be covered here. In this section, we will discuss two more typical flow structures: the flows to drive the particle out of the device (Fig. 12) and the flow structures which could generate a simple shear flow in the central cavity (Fig. 13). The simplest flow structure which could drive the trapped particle out of the device is shown in Fig. 12a, in which M1 is the inlet, M4 is the outlet, and the fluids pass through the device almost straightly ($Q_{\mathrm{M1}} = Q_{\mathrm{M4}} = Q$). Of course, the velocity of flow will reduce in the central cavity due to the area enlargement of the cross-section. If the particle must be guaranteed to retain on the vertical central axis, the flow structure shown in Fig. 12b might be better. Besides M1, both S2 and S3′ are inlets and $Q_{M1} = Q_{\mathrm{S2}} = Q_{\mathrm{S3'}} = (1/3)Q$. The fluids from inlets S2 and S3′ will get into the central cavity from its left and right orifices, respectively, and then converge with the streams from the inlet M1 to form a parallel flow. Under the escort of the right and left streams, the particle in the central streams might be more easily controlled and retain on the central axis.

The flow structures which might lead to a simple shear flow in the central cavity are shown in Fig. 13 in which $Q_{\mathrm{s1'}} = Q_{\mathrm{s2}} = Q_{\mathrm{s3}} = Q_{\mathrm{s4'}} = Q$. Flow direction of the fluids in each channel is shown in Fig. 13a, which is very similar to the rotational flow. The same point for a rotational flow and for flows structures in Fig. 13 is $Q_{\mathrm{s1}}/Q_{\mathrm{s1'}} = Q_{\mathrm{s2'}}/Q_{\mathrm{s2}} = Q_{\mathrm{s3'}}/Q_{\mathrm{s3}} = Q_{\mathrm{s4}}/Q_{\mathrm{s4}}$, while the difference is $Q_{\mathrm{s1}}/Q_{\mathrm{s1'}} = 1$ for a rotational flow, $Q_{\mathrm{s1}}/Q_{\mathrm{s1'}} = 0.3, 0.7, 0.8, 0.9$, and 0.95 for flows in Fig. 13. As shown in Fig. 13b–d, the fluids from inlet S3 (S2) are divided into three groups of streams: the first group leaves the device through the channel of S3′ (S2′); the second passes though the central cavity relatively straight and flows out of the device through S2′ (S4′); and the last group enters the central cavity, which makes a U turn and leaves through S4′ (S1′). Under the action of the second and third group of streams from both S3 and S2, hyperbolic flows are generated in the central cavity. When the ratio $Q_{\mathrm{s1}}/Q_{\mathrm{s1'}}$ increase gradually, the hyperbolic flow gets weaker and weaker. When $Q_{\mathrm{s1}}/Q_{\mathrm{s1'}} = 0.9$ (Fig. 12e), the fluids from inlet S3 (S2) will

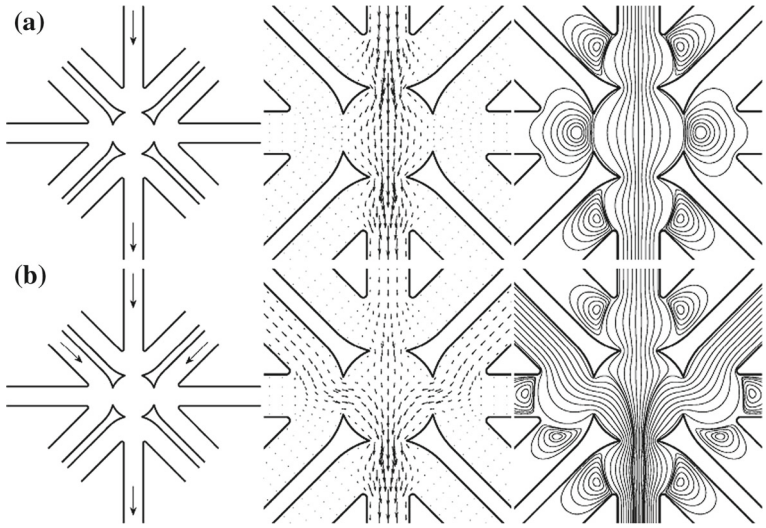

FIG. 12. Flow structures (in terms of velocity vectors and streamlines) to drive the fabricated anisotropic particle out of the device

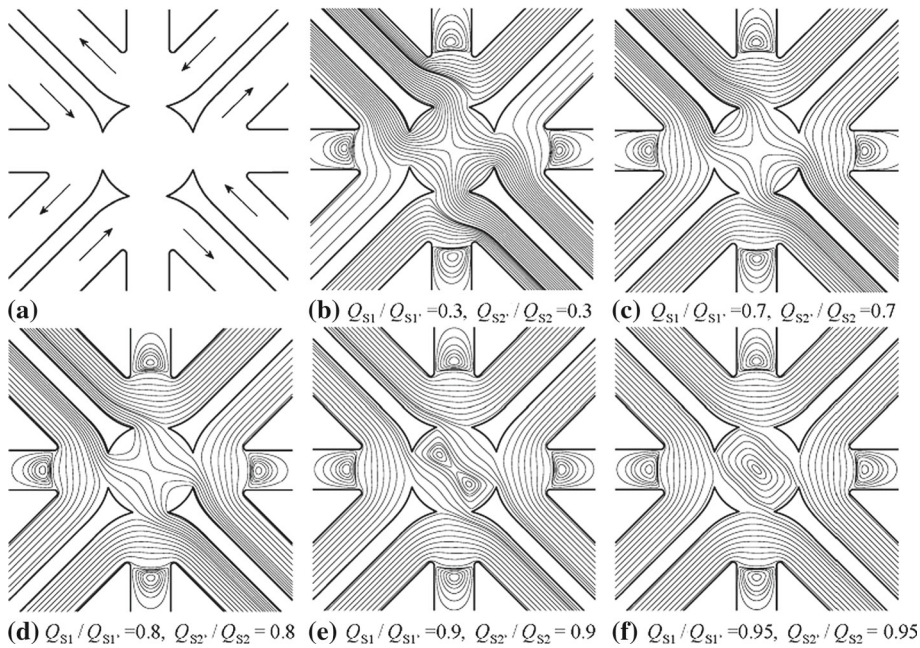

FIG. 13. Flow structures leading to a simple shear flow in the central cavity. **a** Flow direction of the fluids in each channel. **b**–**f** Flow structures in terms of streamlines for various ratios: $Q_{s1}/Qs1' = 0.3, 0.7, 0.8, 0.9$, and 0.95. ($Q_{s1}/Qs1' = Qs2'/Q_{s2} = Qs3'/Q_{s3} = Q_{s4}/Qs4'$)

not make U turn in the central cavity and leave through S4′ (S1′). Under the action of the second group of streams, two small eddies near the center point are generated. Furthermore, when $Q_{s1}/Q_{s1'} = 0.95$ (Fig. 13f), a big elliptical eddy form in the central cavity. The eddy is so flat that the flow field in the vicinity of the center point can be regarded as a shear flow similar to that in Lee et al.'s work [16].

4. Conclusions

A 2D spectral boundary element method is employed to investigate diverse flow structures in a 2D device (CS-MFRM) combining a MFRM and a cross-slot by varying volume flow rates at inlets and outlets of the device. These works strongly support that the boundary element method is a powerful and flexible tool to numerically investigate the problems of interfacial dynamics of Stokes flow in very complex geometries. Especially for the rheology behaviors of droplets in microchannels, the displacement, deformation, and coalescence of droplets are all controlled by the various flow rates into and out of the micro-device, which can be easily reflected in the boundary integral method by simply adjusting the boundary conditions at the inlets and outlets.

Due to the extremely complex geometry of the CS-MFRM, many diverse flow patterns can be generated by controlling the flow rates of the inlets and outlets. As it is unnecessary to investigate every possible flow pattern, we choose several major patterns to analyze in this paper. The flow fields in terms of velocity vectors and streamlines are drawn for different flow structures such as the flow to transport the MD, the extensional flow, the rotational flow, the flow to transport SD, and the simple shear flow. Among them, the extensional flow and the rotational flow are critical in the fabrication process of anisotropic particles. Other flow patterns, such as the propelling flow, can also be employed to achieve some functions like the transport of SD.

The location of the stagnant point similar to that in an extensional flow can be adjusted by controlling the flow rates of the relevant inlets and outlets. This function will be convenient to exactly locate the droplet, especially for the MD.

Eddies in various flow structures investigated in this paper are particularly discussed since they could be used to trap and/or rotate droplets. Similar to Hellou and Bach's results [15], eddies form within branches characterized by low or zero flow. For zero flow rate, the formed eddies occupy the overall width of the branch channel; for low flow rate, the formed eddies are relatively small and only occupy part of the branch channel. The most important eddy is the one generated in the central cavity, which is also called the rotational flow. By employing this big eddy, we can achieve the function to rotate the MD. It is also verified that eddies generated in branches in some flow structures consume many energies of the flows. Thus, flows in a CS-MFRM and a MFRM, such as the rotational flow, might have some difference even if all other conditions are exactly the same.

The geometry of the microchannel also has some effects on the flow structures generated in the micro-device. For instance, in order to generate a simple shear flow, the ratio $Q_{s1}/Q_{s1'} = 0.95$ in our paper, while in Lee et al.'s work [16], this ratio is 0.763. This difference is caused by the different sizes of the orifice of the central cavity for the micro-devices employed by Lee et al. and by us and also by the four eddies formed in the four channels of M1–M4.

Acknowledgments

This work was supported by General Program of Natural Science Foundation of Tianjin (11JCYBJC04300), Major State Basic Research Development Program of China (973 Program) (No. 2012CB720305), National Natural Science Foundation of China (21376162), and National Social Science Foundation of China (09CTJ001).

Appendix: More generalized boundary integral equation (GBIE)

A two-dimensional (2D) multiple-emulsion globule with complex internal structures is located in a microchannel and deforms under the shear of the continuous phase (CP) with viscosity μ and density ρ. S_{ij} indicates the interface of the ijth droplet d_{ij} whose physical parameters are the interface tension γ_{ij}, the

viscosity $\lambda_{ij}\mu$ where λ_{ij} is the viscosity ratio of the ijth droplet to CP, the fluid density $\kappa_{ij}\rho$ where κ_{ij} is the density ratio of the ijth droplet to CP, and the radius $k_{ij}r_{11}$ where r_{11} is the radius of the entire globule and k_{ij} is the radius ratio of the ijth droplet to the globule.

Stokes equations and the continuity equation can also be applied for all droplets of the multiple emulsion. Nonetheless, physical parameters in these equations must be replaced by the corresponding parameters of those droplets, such as the viscosity $\lambda_{ij}\mu$. The subscripts i and j indicate the jth droplet of the ith layer. The interface of the droplet with unit normal vectors $\boldsymbol{n}$ pointing outward is indicated by S_{ij}, and its interface tension is γ_{ij}. Fluid density of the ijth droplet is $\kappa_{ij}\rho$. Boundary conditions (BCs) of the velocity $\boldsymbol{u}$ and surface stress $\mathbf{f}$ on S_{ij} are

$$\boldsymbol{u}_{i,j} = \boldsymbol{u}_{i,j}^{ijmom}, \tag{13}$$

$$\begin{aligned}\Delta \boldsymbol{f}_{i,j} &= \boldsymbol{f}_{i,j}^{ijmom} - \boldsymbol{f}_{i,j} \\ &= \gamma_{i,j}\left(\nabla\cdot\boldsymbol{n}\right)\boldsymbol{n} + \left(\kappa^{ijmom} - \kappa_{i,j}\right)\rho\left(\boldsymbol{g}\cdot\boldsymbol{x}\right)\boldsymbol{n}, \\ &\quad (i = 1, 2, \ldots\ldots, n; \quad j = 1, 2, \ldots\ldots, m_i)\end{aligned} \tag{14}$$

where $\boldsymbol{g}$ is the gravity acceleration, and the superscript "ijmom" indicates the mother droplet of the ijth droplet (when $i = 1$, "ijmom" indicates CP). At walls (S_0) of the microchannel, the non-slip BC (Eq. 5) is employed. At the inlets and outlets (S_0) of the cross-slot, the undisturbed flows which are specified as the parabolic pressure-driven flows (Eq. 6) are employed. The velocity at a point $\boldsymbol{x}_0$ on the droplet surface S_{ij} and outer boundaries S_0 can be described by the more generalized boundary integral equation (GBIE) [32,33]

$$\begin{aligned}\mathrm{LHS} = &-\int_{S_0}[\boldsymbol{S}\cdot\boldsymbol{f} - \mu\boldsymbol{T}\cdot\boldsymbol{u}\cdot\boldsymbol{n}]\mathrm{d}S \\ &-\sum_{j=1}^{m_1}\int_{\boldsymbol{S}_{1,j}}[\boldsymbol{S}\cdot\Delta\boldsymbol{f}_{1,j} - (1-\lambda_{1,j})\mu\boldsymbol{T}\cdot\boldsymbol{u}\cdot\boldsymbol{n}]\mathrm{d}S \\ &-\sum_{i=2}^{n}\sum_{j=1}^{m_i}\int_{S_{i,j}}[\boldsymbol{S}\cdot\Delta\boldsymbol{f}_{i,j} - (\lambda^{ijmom}-\lambda_{i,j})\mu\boldsymbol{T}\cdot\boldsymbol{u}\cdot\boldsymbol{n}]\mathrm{d}S\end{aligned} \tag{15}$$

where LHS is given by

$$\begin{aligned}\mathrm{LHS} = &\begin{cases}2\pi\mu\boldsymbol{u}(\boldsymbol{x}_0) & \boldsymbol{x}_0\in\boldsymbol{S}_0 \\ 2\pi\mu(1+\lambda_{1,j})\boldsymbol{u}(\boldsymbol{x}_0) & \boldsymbol{x}_0\in\boldsymbol{S}_{1,j} \\ 2\pi\mu(\lambda^{ijmom}+\lambda_{i,j})\boldsymbol{u}(\boldsymbol{x}_0) & \boldsymbol{x}_0\in\boldsymbol{S}_{i,j},\end{cases} \\ &(i = 2, 3, \ldots\ldots n-1, n \\ &j = 1, 2, 3, \ldots\ldots m_i - 1, m_i)\end{aligned} \tag{16}$$

where n, m_1, and m_i can be any integer. $\boldsymbol{S}$ is the fundamental solution of the two-dimensional Stokes equations and $\boldsymbol{T}$ is the associated stress kernel.

When $n = 1$ and m_1 is any positive integer, they are BIEs to study the deformation and coalescence of simple droplets of any numbers (Eq. 7). When $n = 2, m_1 = 1$, and $m_2 = 1$, Eqs. 15 and 16 are simplified to Eqs. 17 and 18 to treat core-shell double emulsions,

$$\begin{aligned}\mathrm{LHS} = &-\int_{S_0}[\boldsymbol{S}\cdot\boldsymbol{f}-\mu\boldsymbol{T}\cdot\boldsymbol{u}\cdot\boldsymbol{n}]\mathrm{d}S\\ &-\int_{S_{1,1}}[\boldsymbol{S}\cdot\Delta\boldsymbol{f}_{1,1}-(1-\lambda_{1,1})\mu\boldsymbol{T}\cdot\boldsymbol{u}\cdot\boldsymbol{n}]\mathrm{d}S\\ &-\int_{S_{2,1}}[\boldsymbol{S}\cdot\Delta\boldsymbol{f}_{2,1}-(\lambda_{1,1}-\lambda_{2,1})\mu\boldsymbol{T}\cdot\boldsymbol{u}\cdot\boldsymbol{n}]\mathrm{d}S\end{aligned} \tag{17}$$

where LHS is given by

$$\mathrm{LHS} = \begin{cases} 2\pi\mu\boldsymbol{u}(\boldsymbol{x}_0) & \boldsymbol{x}_0\in\boldsymbol{S}_0\\ 2\pi\mu(1+\lambda_{1,1})\boldsymbol{u}(\boldsymbol{x}_0) & \boldsymbol{x}_0\in\boldsymbol{S}_{1,1}\\ 2\pi\mu(\lambda_{1,1}+\lambda_{2,1})\boldsymbol{u}(\boldsymbol{x}_0) & \boldsymbol{x}_0\in\boldsymbol{S}_{2,1}.\end{cases} \tag{18}$$

S_0 in Eqs. 15 and 17 could be any actual channels with diverse geometries. It also could be any virtual boundaries which never exist in the actual flow fields. For the latter, when S_0 is far away from the globule, Eqs. (15, 16) and (17, 18) can be used to treat globules in an infinite flow approximately, such as the infinite extensional flow. The infinite extensional flow $\boldsymbol{u}^\infty$ employed by Stone and Leal [35] is

$$\boldsymbol{u}^\infty = \frac{1}{2}G\begin{pmatrix}-1 & 0 & 0\\ 0 & -1 & 0\\ 0 & 0 & 2\end{pmatrix}\boldsymbol{x}. \tag{19}$$

By repeating the results of Stone and Leal [35] for the deformation of a concentric double-emulsion globule under an axisymmetric extensional flow, we can validate our numerical model and code.

References

1. Helen, S., Delai, L.C., Rustem, F.I.: Reactions in droplets in microfluidic channels. Angew. Chem. Int. Ed. **45**, 7336–7356 (2006)
2. Whitesides, G.M.: The origins and the future of microfluidics. Nature **442**, 368–373 (2006)
3. Teh, S.Y., Lin, R., Hung, L.H., Lee, A.P.: Droplet microfluidics. Lab Chip **8**, 198–220 (2008)
4. Wang, J.T., Wang, J., Han, J.J.: Fabrication of advanced particles and particle-based materials assisted by droplet-based microfluidics. Small **7**, 1728–1754 (2011)
5. Lingxin, C., Sangyeop, L., Jaebum, K.L., Eun, C.: Continuous dynamic flow micropumps for microfluid manipulation. J. Micromech. Microeng. **18**, 013001 (2008)
6. Um, E., Park, J.K.: A microfluidic abacus channel for controlling the addition of droplets. Lab Chip **9**, 207–212 (2009)
7. Dendukuri, D., Doyle, P.S.: The synthesis and assembly of polymeric microparticles using microfluidics. Adv. Mater. **21**, 1–16 (2009)
8. Aubin, J., Ferrando, M., Jiricny, V.: Current methods for characterising mixing and flow in microchannels. Chem. Eng. Sci. **65**, 2065–2093 (2010)
9. Hao, G., Michel, H.G.D., Frieder, M.: Droplets formation and merging in two-phase flow microfluidics. Int. J. Mol. Sci. **12**, 2572–2597 (2011)
10. Seemann, R., Brinkmann, M., Pfohl, T., Herminghaus, S.: Droplet based microfluidics. Rep. Prog. Phys. **75**, 016601 (2012)
11. Tanyeri, M., Johnson-Chavarria, E.M., Schroeder, C.M.: Hydrodynamic trap for single particles and cells. Appl. Phys. Lett. **96**, 224101 (2010)
12. Janssen, J.J.M., Boon, A., Agterof, W.G.M.: Influence of dynamic interfacial properties on droplet breakup in plane hyperbolic flow. AICHE J. **43**, 1436–1447 (1997)
13. Perkins, T.T., Smith, D.E., Chu, S.: Single polymer dynamics in an elongational flow. Science **276**, 2016–2021 (1997)
14. Schroeder, C.M., Babcock, H.P.E., Shaqfeh, S.G., Chu, S.: Observation of polymer conformation hysteresis in extensional flow. Science **301**, 1515–1519 (2003)
15. Hellou, M., Bach, T.D.P.: Stokes flow in a junction of two-dimensional orthogonal channels. Z. Angew. Math. Phys. **62**, 135–147 (2011)

16. Lee, J.S., Dylla-Spears, R., Teclemariam, N.P., Muller, S.J.: Microfluidic four-roll mill for all flow types. Appl. Phys. Lett. **90**, 074103 (2007)
17. Wang, J.T., Han, J.J., Yu, D.M.: Numerical studies of geometry effects of a two-dimensional microfluidic four-roll mill on droplet elongation and rotation. Eng. Anal. Bound. Elem. **36**, 1453–1464 (2012)
18. Lee, J.S., Shaqfeh, E.S.G., Muller, S.J.: Dynamics of DNA tumbling in shear to rotational mixed flows: pathways and periods. Phys. Rev. E **75**, 040802 (2007)
19. Deschamps, J., Kantsler, V., Segre, E., Steinberg, V.: Dynamics of a vesicle in general flow. PNAS **106**, 11444–11447 (2009)
20. Young, Y.N., Blawzdziewicz, J., Cristini, V., Goodman, R.H.: Hysteretic and chaotic dynamics of viscous drops in creeping flows with rotation. J Fluid Mech. **607**, 209–234 (2008)
21. Wang, J.T., Tao, J., Han, J.J.: Hydrodynamic Control of Droplets Coalescence in Microfluidic Devices to Fabricate Anisotropic Particles Through Boundary Element Method (unpublished)
22. Shankar, P.N.: The eddy structure in Stokes flow in a cavity. J. Fluid Mech. **250**, 371–383 (1993)
23. Georgiadou, M., Mohr, R., Alkire, R.C.: Local mass transport in two-dimensional cavities in laminar shear flow. J. Electrochem. Soc. **147**, 3021–3028 (2000)
24. Lutz, B.R., Chen, J., Schwartz, D.T.: Hydrodynamic Tweezers: 1. Non-contact cell trapping in a laminar oscillating flow. Anal. Chem. **78**, 5429–5435 (2006)
25. Lin, C.M., Lai, Y.S., Liu, H.P., Chen, C.Y., Wo, A.M.: Trapping of bioparticles via microvortices in a microfluidic device for bioassay applications. Anal. Chem. **80**, 8937–8945 (2008)
26. Pozrikidis, C.: Boundary Integral and Singularity Methods for Linearized Viscous Flow. Cambridge University Press, Cambridge (1992)
27. Youngren, G.K., Acrivos, A.: On the shape of a gas bubble in a viscous extensional flow. J Fluid Mech. **76**, 433–42 (1976)
28. Muldowney, G.P., Higdon, J.J.L.: A spectral boundary element approach to three-dimensional Stokes flow. J. Fluid Mech. **298**, 167–192 (1995)
29. Liang, J., Subramaniam, S.: Computation of molecular electrostatics with boundary element methods. Biophys. J. **73**, 1830–1841 (1997)
30. Pozrikidis, C.: Interfacial dynamics for Stokes flow. J Comput. Phys. **169**, 250–301 (2001)
31. Dimitrakopoulos, P., Wang, J.T.: A spectral boundary element algorithm for interfacial dynamics in two-dimensional Stokes flow based on Hermitian interfacial smoothing. Eng. Anal. Bound. Elem. **31**, 646–656 (2007)
32. Wang, J.T., Liu, J.X., Han, J.J., Guan, J.: Effects of complex internal structures on rheology of multiple emulsions particles in 2D from a boundary integral method. Phys. Rev. Lett. **110**, 066001 (2013)
33. Wang, J.T, Liu, J.X., Han, J.J., Guan, J.: Rheology investigation of the globule of multiple emulsions with complex internal structures through a boundary element method. Chem. Eng. Sci. **96**, 87–97 (2013)
34. Baroud, C.N., Gallaire, F., Dangla, R.: Dynamics of microfluidic droplets. Lab Chip **10**, 2032–2045 (2010)
35. Stone, H.A., Leal, L.G.: Breakup of concentric double emulsion droplets in linear flows. J Fluid Mech. **211**, 123–156 (1990)

Jing Guan
School of Science
Tianjin University
Tianjin 300072
People's Republic of China

Jinxia Liu, Xiaoduan Li, Jun Tao and Jingtao Wang
School of Chemical Engineering and Technology
Tianjin University
Tianjin 300072
People's Republic of China
e-mail: wjingtao928@tju.edu.cn

Jingtao Wang
State Key Laboratory of Chemical Engineering
Tianjin University
Tianjin
People's Republic of China

(Received: January 5, 2013; revised: December 25, 2013)